

# Finite element modeling of machining-induced microstructure evolution of IN625 superalloy fabricated by laser-based powder bed fusion

*Binxun Li*<sup>1 2\*</sup>, *Yan Xia*<sup>1 2</sup>, and *Bin Fang*<sup>1 2</sup>

<sup>1</sup>School of Mechanical Engineering, Qilu University of Technology (Shandong Academy of Sciences), Jinan, China

<sup>2</sup> Shandong Institute of Mechanical Design and Research, Jinan, China

**Abstract.** The surface quality of components fabricated via laser-based powder bed fusion (L-PBF) is highly dependent on the post-machining technique. This study aims to investigate the microstructure evolution of the turning-affected subsurface layer of the IN625 superalloy manufactured by L-PBF with the assistance of the finite element analysis (FEA). A finite element model with integrated user-defined subroutine VUSDFLD was created for numerical modeling of the dislocation density and grain size evolution due to turning operation. The simulation results regarding grain size and the depth of the affected layer were validated against the experiments. This study shed some light on the metallurgical behavior evolution when turning of L-PBF of nickel-based superalloy based on the proposed material microstructure model.

## 1 Introduction

Additive manufacturing (AM) is one of the advanced manufacturing technologies utilized to fabricate components with intricate free surfaces in a feasible way. As one of the powerful and most commonly used AM processes, laser-based powder bed fusion (L-PBF) has demonstrated great potential in producing integrated and complex metal components in the fields of aerospace, bio-medical, automotive, etc [1, 2]. Regarding the L-PBF processes, the metal powder particles are laid and melted layer by layer with laser heat source scanning along designated routes. As a result, the fabricated metal components always show rough surfaces, low dimensional precision, and other surface defects, which makes it hard to meet the practical requirements [3,4]. Therefore, the post-machining technique including turning has been taken as an efficient way to deal with the poor surface quality resulting from the L-PBF process.

IN625 is a Ni-based superalloy with chemical elements Mo and Ni as the solution-strengthening precipitates. Due to its attractive mechanical properties including high-temperature strength, high corrosion resistance, and creep resistance, IN625 has been broadly used to manufacture components applied to the aerospace field [5]. Taking the advantages of L-PBF, the Ni-based components with high geometrical complexity can be easily fulfilled.

---

\* Corresponding author: [libx@qlu.edu.cn](mailto:libx@qlu.edu.cn)

However, the L-PBF of IN625 superalloy features with remarkably anisotropic microstructure and properties different from wrought Ni-based superalloy determines the difficulty in turning processes [6]. Fei et al. [7] studied the machinability of L-PBF manufactured IN625 in terms of cutting force, tool wear, and chip morphology as well as surface finish with scanning strategy as variables. Patel et al. [8] further discussed the cutting direction and scan strategy rotation on milling force which is attributed to the physical parameter and microstructure. Yang et al. [9] pointed out that the surface morphology and surface integrity are affected by the relative orientation of the cutting direction to the build direction and scan strategy rotation. Moreover, several researchers conducted studies to compare the machinability between L-PBF of nickel-based alloys and wrought alloys regarding tool wear, surface defect, chip morphology, etc [10-13]. Considering the non-homogeneous microstructure, the metallurgical behavior in the machined surface is another important aspect attracting great attention. However, there is limited relevant research concerning machining-induced microstructure evolution. Ji et al. [14] found slight grain coarsening and texture weakening in the micro-milling of L-PBF IN718 in contrast with strong grain coarsening for wrought IN718. Careri et al. [15] observed severe plastic deformation beneath the machined surface and based on the EBSD map, a high concentration of dislocation density and local misorientation was revealed in the affected layer. A similar investigation performed by Taşcıoğlu et al. [16] also confirmed the obvious plastic deformation. More in detail, the surface cellular grain as well as its boundary just below the machined surface can barely be recognized. Since the mechanical property is the reflection of microstructure, an in-depth investigation of the machining-induced transformation of metallurgical behavior is crucial. Meanwhile, the finite element method (FEM) provides an efficient and feasible method to capture the microstructure evolution during machining.

In this study, a dislocation density-based material model was developed and then integrated into the created FE cutting simulation model to reveal the grain refinement visibly. Experimental results obtained through OM, SEM, and EBSD characterization techniques were provided for simulation comparison and verification.

## 2 Dislocation density-based model

A dislocation density-based material model was adopted to model the cell structure formation and the induced grain refinement. It assumed that the grain refinement in the machined subsurface is considered to be induced by the dislocation pile-up and tangle. In this material model, it consists of different types of dislocation density including the cell interior dislocation density ( $\rho_c$ ) and the cell wall dislocation density ( $\rho_w$ ). The grain size ( $d$ ) can be calculated as a function of the total dislocation density ( $\rho_{tot}$ ). More information regarding the material model can be found in Ref.[17], while the main equations are given as follows:

$$\dot{\rho}_c = \alpha^* \frac{1}{\sqrt{3}b} \sqrt{\rho_w} \dot{\gamma}_w^r - \beta^* \frac{6}{bd(1-f)^{1/3}} \dot{\gamma}_c^r - k_0 \left( \frac{\dot{\gamma}_c^r}{\dot{\gamma}_0} \right)^{-1/n} \rho_c \dot{\gamma}_c^r \quad (1)$$

$$\dot{\rho}_w = \beta^* \frac{\sqrt{3}(1-f)}{fb} \sqrt{\rho_w} \dot{\gamma}_c^r + \beta^* \frac{6(1-f)^{2/3}}{bdf} \dot{\gamma}_c^r - k_0 \left( \frac{\dot{\gamma}_w^r}{\dot{\gamma}_0} \right)^{-1/n} \rho_w \dot{\gamma}_w^r \quad (2)$$

$$\rho_{tot} = f \rho_w + (1-f) \rho_c \quad (3)$$

$$d = K / \sqrt{\rho_{tot}} \quad (4)$$

### 3 Experimental procedure and finite element modeling

#### 3.1 Turning experiment

The turning experiments of the L-PBF of IN625 were performed on a CNC lathe using a coated cemented carbide cutting insert (CNMG120408-M5, Seco, Sweden). The cutting insert was mechanically mounted on a matchable tool holder, which provides a rake angle of  $-6^\circ$  and a clearance angle of  $0^\circ$ . The cutting speed is 60 m/min, and the feed and radial depth of the cut are 0.102 mm and 0.3 mm. After turning the experiment, the specimen was cut out from the cylinder bar and then subjected to mosaic, grinding, polishing, and etching for cross-section metallurgical observation. Detailed information about the turning and post-processing is shown in Fig. 1.

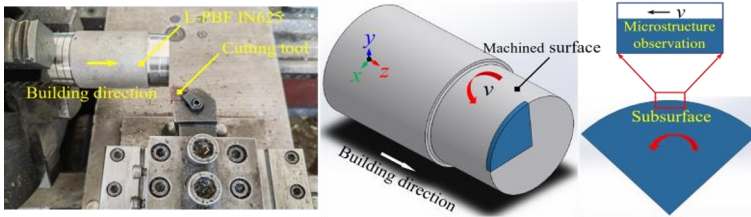


**Fig. 1.** Turning experiments of L-PBF of IN625 and microstructure observation.

#### 3.2 FE numerical procedure

During the turning simulation, the most commonly used Johnson-Cook material constitutive model was employed to describe the material shear plastic flow behavior (Eq.4) [18]. Correspondingly, the Johnson-Cook shear damage model was utilized to describe the material failure and chip formation (Eq.5) [19]. Detailed information about the Johnson-Cook constitutive model and shear damage model constants is listed in Table 1 and Table 2.

$$\sigma = (A + B\varepsilon^n) \left[ 1 + C \ln \left( \frac{\dot{\varepsilon}}{\dot{\varepsilon}_0} \right) \right] \left[ 1 - \left( \frac{T - T_r}{T - T_m} \right)^m \right] \quad (5)$$

$$\varepsilon_f^{pl} = [d_1 + d_2 \exp(-d_3)\eta] \left[ 1 + d_4 \ln \left( \frac{\dot{\varepsilon}^{pl}}{\dot{\varepsilon}_0} \right) \right] (1 - d_5 \tilde{\theta}) \quad (6)$$

**Table 1.** Johnson-Cook constitutive model parameters for L-PBF of IN625 [20,21].

$A$ (MPa)	$B$ (MPa)	$n$	$C$	$m$	$\dot{\varepsilon}_0$ (s $^{-1}$ )	$T_0$ ( $^\circ$ C)	$T_m$ ( $^\circ$ C)
709	2366	0.726	0.000209	1.56	1670	25	1350

**Table 2.** Johnson-Cook shear damage model parameters [22,23].

$d_1$	$d_2$	$d_3$	$d_4$	$d_5$
0.04	0.75	-1.45	0.04	0.89

Fig. 1 shows the created 2D FE model for turning IN625. Table 3 lists the primary thermo-mechanical properties of IN625. The domain used is a rectangle of dimensions 4 mm  $\times$  1.8 mm. To improve the efficiency of computation and guarantee the simulation accuracy, the domain was partitioned into two parts and the element size with bias control and no bias was applied to the bottom zone and top zone, respectively. A total of 16600 elements and 653 elements were meshed corresponding to the workpiece and tool insert. The element type of

CPE4RT features with coupled temperature-displacement was assigned to the workpiece and tool insert. The cutting insert was considered a rigid body. As far as the boundary condition is concerned, the bottom of the workpiece was fixed and the cutting insert was set to move along the x-direction at a constant cutting speed of 60 m/min.

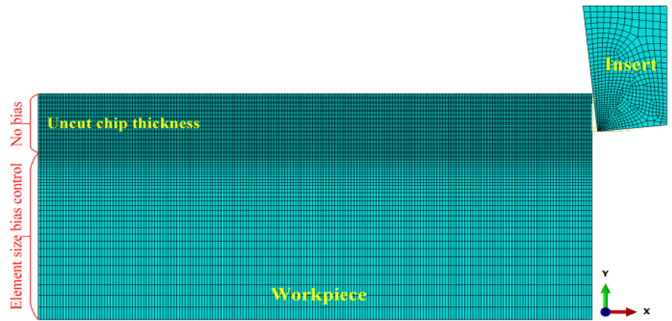


**Fig. 2.** 2D FE model for turning of IN625.

**Table 3.** Thermo-physical properties of IN625 alloy.

Density (kg/m <sup>3</sup> )	Young's modulus (MPa)	Poisson's ratio	Conductivity (W/m/°C)	Thermal expansion (1/°C)	Specific heat (J/kg/°C)
8440	205	0.308	12.1	1.23e-5	478

### 4 Results and discussion

Fig.3 shows the simulated dislocation density and grain size evolution in the machined surface layer. From Fig.3(a), the dislocation density starts at a large value of around  $1.3 \times 10^9 \text{mm}^{-2}$  from the top-most machined surface and then decreases as the depth increases until reaches the initial value of the specimen. Similarly, the predicted grain size exhibits a minimum value of about  $0.5 \mu\text{m}$  on the top surface and increases progressively to  $1.47 \mu\text{m}$ . It can be anticipated that greater dislocation density induced by machining resulted in the grain size refinement. The affected depth is around  $300 \mu\text{m}$  according to Fig. 3(c).

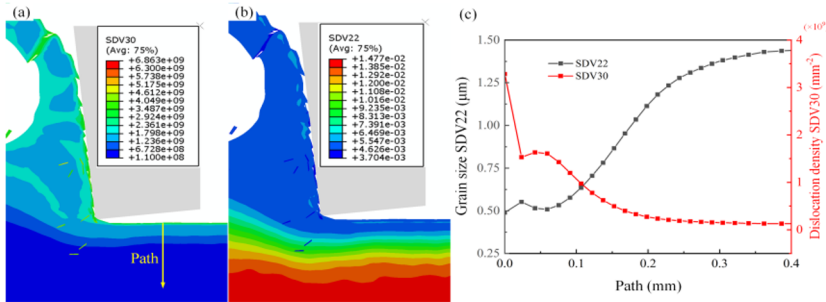


**Fig. 3.** Predicted results: (a) dislocation density, (b) grain size, (3) variation along the path.

The subsurface microstructure of L-PBF manufactured IN625 after turning is shown in Fig.4. Similar to previous findings in the machining of wrought nickel-based superalloy, a prominent dark layer is observed beneath the top-most machined surface [24,25], with the affected depth layer varies in the range of  $75 \sim 93 \mu\text{m}$ . Additionally, a thin white layer with thicknesses of approximately  $3.5 \mu\text{m}$  is generated. The microstructure beneath the machined surface exhibits a non-homogeneous composition of dendritic and cellular grains, as confirmed in Fig. 4(b). Slip lines indicating grain deformation and reorientation are marked

with yellow dashed lines. The machining-induced slip traces within the grain boundary have been found to cause changes in grain crystallographic orientation [26], which will be further discussed based on EBSD analysis. In Fig. 4(b), the microstructure in the white layer has evolved into a more homogeneous structure, exhibiting amorphous characteristics without clear grain boundaries.

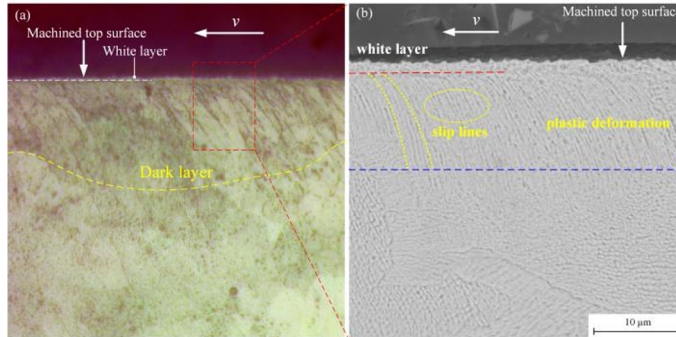


**Fig. 4.** Machined subsurface observation: (a) optical image, (b) SEM.

Fig. 4 shows the EBSD image of the machined surface layer. As shown in Fig. 5(a), the grain boundaries are tilted and elongated along the cutting direction. More in detail, smaller grain was formed in the subsurface. In addition, the grain of L-PBF of IN625 presents a large size and the crystallographic orientation beneath the top machined surface shows grain orientation evolution even interior of the grain. In Fig. 5(b), the KAM map is a qualitative reflection of dislocation density with a maximum depth of around 70 µm and also the colour changes from yellow to blue as the distance increases along the path suggests the dislocation density descending referring to the legend, which verified the predicted dislocation density accumulation. The red lines in Fig. 5(c) indicate the sub-grain boundary formation due to dislocation migration.

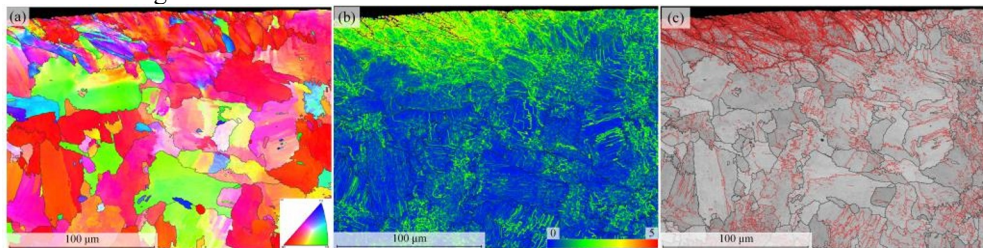


**Fig. 5.** EBSD characterization: (a) optical image, (b) SEM.

## 5 Conclusions

In this study, the FE cutting simulation of L-PBF of IN625 with an integrated dislocation density-based material model was conducted to explore the grain refinement validated against experimental results. The main conclusions are as follows:

(1) The dislocation density evolution and grain refinement were captured in the machined surface layer of IN625 manufactured via L-PBF by integrating the dislocation density-based material model.

(2) A white layer in a depth of 3.5 µm showing amorphous microstructure was formed beneath the top-most machined surface followed by the produced dark layer showing plastic deformation with affected depth in the range of 75~93µm.

(3) The EBSD image validated the simulation results concerning dislocation density and grain size qualitatively.

As an extension of this work, how to take the non-homogeneous microstructure of L-PBF manufactured IN625 into consideration to more accurately capture the microstructure evolution is ongoing by the authors' team.

This work was supported by the Natural Science Foundation of Shandong Province (Grant No. ZR2021QE230), the Talent Research Project of Qilu University of Technology (Shandong Academy of Sciences) (No. 2023RCKY118), the National Natural Science Foundation of China (Grant No. 52205480 and No. 52275438).

## References

1. K. Kanishka, B. Acherjee, *J. Manuf. Processes* **107** (2023).
2. Z. Tian, C. Zhang, D. Wang, W. Liu, Y. Tian, *Appl. Sci.* **10**, 1 (2019).
3. P. Zhang, Z. Liu, J. Du, G. Su, J. Zhang, C. Xu, *J. Manuf. Processes* **53** (2020).
4. Sen, C. Subasi, L. Ozaner, O. C. *CIRP Conference on Surface Integrity* **87** (2020).
5. M. Yakout, M.A. Elbestawi, S.C. Veldhuis, *Solid State Phenom.* **278** (2018).
6. K.D. Ramkumar, W.S. Abraham, V. Viyash, N. Arivazhagan, A.M. Rabel, *J. Manuf. Processes* **25** (2017).
7. J. Fei, G. Liu, K. Patel, T. Ozel, *J. Manuf. Mater. Process.* **4**, 2 (2020).
8. K. Patel, J. Fei, G. Liu, T. Ozel, *Prod. Eng.* **13**, 2 (2019).
9. L. Yang, K.V. Patel, K. Jarosz, *CIRP Conference on Surface Integrity.* **87** (2020).
10. T. Ostra, U. Alonso, F. Veiga, M. Ortiz, P. Ramiro, A. Alberdi, *Mater.* **12**, 13 (2019).
11. L. Chen, Q. Xu, Y. Liu, G. Cai, J. Liu, *Int. J. Adv. Manuf. Technol.* **114** (2020).
12. L. Shu, X. Cang, J. Zhou, Z. Heng, H. Wu, W. He, *Mater. Today Commun.* **34** (2023).
13. H. Salvi, H. Vesuwala, P. Raval, V. Badheka, N. Khanna, *Sustainable Mater. Technol.* **35** (2023).
14. H. Ji, M.K. Gupta, Q. Song, W. Cai, T. Zheng, Y. Zhao, Z. Liu, D.Y. Pimenov, *J. Mater. Res. Technol.* **14** (2021).
15. F. Careri, S. Imbrogno, D. Umbrello, M.M. Attallah, J. Outeiro, A.C. Batista, *J. Manuf. Processes* **61** (2021).
16. E. Tacolu, Y. Kaynak, S. Sharif, F. Ptr, M.A. Suhaimi, *Mach. Sci. Technol.* **26(1)** (2022).
17. H. Ding, N. Shen, Y.C. Shin, *Comput. Mater. Sci.* **50** (2011).
18. G.R. Johnson, W.H. Cook, *Eng. Fract. Mech.* **21** (1985).
19. O. Pantalé, J.L. Bacaria, O. Dalverny, R. Rakotomalala, S. Caperaa, **193**, (39–41) (2004).
20. M. Hokka, D. Gomom, A. Shrot, T. Leemet, M. Bäker, V.T. Kuokkala, *Exp. Mech.* **54**, 2 (2014).
21. M.M. Lotfi, Jahanbakhsh, A.A. Farid, *Tribol. Int.* **99** (2016).
22. W. Xie, F. Yang, L. Ding, F. Scarpa, *Mater. Des.* **182** (2019).
23. B. Erice, F. Gálvez, *Int. J. Solids Struct.* **51**, 1 (2014).
24. Du J, Lv S, *Appl. Surf. Sci.* **292** (2014).
25. S. Zhang, Z. Liu, B. Wang, X. Ren, A.M. Khan, M. Zhao, *J. Mater. Res. Technol.* **15** (2021).
26. L. Li, H. Chen, Z. Liao, Y. Yang, D. Axinte, *Int. J. Mach. Tools Manuf.* **190** (2023).